The DOI for this manuscript is doi: 10.1175/BAMS-D-13-00276.1

The IITM Earth System Model: Transformation of a Seasonal Prediction Model to a Long Term Climate Model

P. Swapna[1], M. K. Roxy[1], K. Aparna[1], K. Kulkarni[1,2], A. G. Prajeesh[1], K. Ashok[1,4*], R. Krishnan[1], S. Moorthi[3], A. Kumar[3] and B. N. Goswami[1]

[1]Centre for Climate Change Research, Indian Institute of Tropical Meteorology, Pune, India

[2] Max Planck Institute for Meteorology, Germany

[3]National Centre for Environmental Prediction, NOAA, USA

[4]*Presently at* UCESS, University of Hyderabad, India

Corresponding Author:
Ashok Karumuri
Centre for Climate Change Research
Indian Institute of Tropical Meteorology, Pune, India
E-mail : ashok@tropmet.res.in

Abstract

With the goal of building an Earth System Model (ESM) appropriate for detection, attribution and projection of changes in the South Asian monsoon, a state-of-the-art seasonal prediction model, namely the Climate Forecast System version 2 (CFSv2) has been adapted to a climate model suitable for extended climate simulations at the Indian Institute of Tropical Meteorology (IITM), Pune, India. While the CFSv2 model has been skillful in predicting the Indian summer monsoon (ISM) on seasonal time scales, a century-long simulation with it shows biases in the ocean mixed-layer, resulting in a 1.5ºC cold bias in the global mean surface air temperature, a cold bias in the sea surface temperature (SST) and a cooler-than-observed troposphere. These biases limit the utility of CFSv2 to study climate change issues. To address biases, and to develop an Indian Earth System Model (IITM-ESMv1), the ocean component in CFSv2 was replaced at IITM with an improved version, having better physics and an interactive ocean biogeochemistry. A 100-year simulation with the new coupled model (with biogeochemistry switched off) shows substantial improvements, particularly in global mean surface temperature, tropical SST and mixed layer depth. The model demonstrates fidelity in capturing the dominant modes of climate variability such as the ENSO and Pacific Decadal Oscillation. The ENSO-ISM teleconnections and the seasonal lead-lags are also well simulated. The model, a successful result of the Indo-US collaboration, will contribute to the IPCC-AR6 simulations, a first from India.

Capsule Summary

This work documents the fidelity of the newly-developed IITM climate model simulations, and demonstrates its suitability to address the climate variability and change issues relevant to South Asian Monsoon.

1. Introduction

The Ministry of Earth Sciences, Govt. of India and National Ocean and Atmospheric Administration (NOAA), USA entered into a formal agreement for collaboration to implement the NCEP weather and seasonal prediction system in India in 2011. Under this collaboration, the India Meteorology Department (IMD) and National Centre for Medium Range Weather Forecasts (NCMRWF) implemented the high resolution (T574, L64) atmospheric Global Forecasting System (GFS) model with 3-DVar data assimilation at IMD for short and medium range weather forecasts. Also, the coupled ocean-atmosphere model, Climate Forecast System version 2 (CFSv2) model with a high resolution atmosphere (T382, L64) was implemented for seasonal prediction at the Indian Institute of Tropical Meteorology (IITM). To address the long term critical need in India for a climate model that would provide reliable future projections of Indian monsoon rainfall, IITM planned to build an Earth System Model (ESM) based on the CFSv2 framework. Further, under the Monsoon Mission (see http://www.tropmet.res.in/) India is committed to improve the CFSv2 model for providing more skillful predictions of seasonal monsoon rainfall, which would also benefit the short and medium range predictions at IMD. Therefore, the extension of the seasonal prediction model to a long term climate model would establish a seamless prediction system from weather time scales to seasonal and decadal time scales in India. In this paper, we describe how the seasonal prediction model has been converted to a model suitable for long term climate studies.

The NCEP CFS (Saha et al. 2006), the predecessor of the CFSv2, used to provide coupled ocean-atmospheric forecasts since 2004, demonstrated good skill in simulating and predicting ENSO (Wang et al. 2005; Zhang et al. 2007), and the South Asian summer monsoon variability (Achuthavarier and Krishnamurthy 2010; Yang et al. 2008; Pattanaik and Kumar 2010; Chaudhari et al. 2013; Pokhrel et al. 2012, 2013). With substantial changes compared to CFSv1, the CFSv2 (Saha et al. 2013) demonstrated better prediction skills for ENSO, the tropical Atlantic sea surface temperatures (SST), global land precipitation, surface air temperature, and the Madden–Julian Oscillation (Yuan et al. 2011; Weaver et al. 2011; Jiang et al. 2013; Hu et al. 2012). Importantly, exhaustive hindcast experiments on seasonal and extended timescales carried out at IITM demonstrated that the CFSv2 model was one of the few models that predicted the general distribution of Indian summer monsoon rainfall during June through September (henceforth ISMR) and its intraseasonal and interannual variability with statistically significant skill (Roxy et al. 2012; Chaudhari et al. 2013).

To address issues related to longer time-scale climate variability, beyond the seasonal time-scale, a climate model needs to simulate the observed mean climate reasonably well. Moreover, for a region like South Asia, a realistic simulation of the climatology and variability of the ISM and the drivers of its variability is imperative. Equally important is the ability to replicate the observed sensitivity in temperature to the increasing greenhouse gases (GHGs). However, despite its good seasonal prediction skill, several 100-year simulations carried out at IITM demonstrated a cold bias in global mean temperature and a lack of the observed sensitivity to GHG increase in CFSv2, limiting its utility as a climate change model (e.g. Roxy et al. 2012). The model also exhibits a dry bias over Indian subcontinent during the June-September (JJAS) monsoon season, along with a colder-than-observed SST in the Arabian Sea (Roxy et al. 2012), and eastern tropical Indian Ocean (Chaudhari et al. 2013). Roxy et al., (2012) also noticed a systematic bias in the thickness of the mixed layer in the ocean component of CFSv2. While model systematic biases tend to affect the simulation of long-term mean climate as well as long-term projected trends, improved representation of oceanic processes is one approach towards minimizing systematic biases (see Semtner and Chervin, 1992). For example, such an effort has substantially improved the simulation of many key climate features in GFDL CM2.5 (Delworth et al. 2012), a state of the art model. These works provide motivation for possible alleviation of systematic biases in the CFSv2 model through improved representation of ocean processes in the coupled model.

As the first step towards adapting the CFSv2 as an ESM, an ocean model with biogeochemistry, and a better physics for improving the biases of the current ocean component in CFSv2 was incorporated. In this study, we document the formulation of the IITM-Earth System Model version 1 (IITM-ESMv1), and discuss improvements in simulations of various important ocean-atmospheric processes, and variability.

The paper is organized as follows. Section 2 describes the model configuration, coupling strategy, experimental design, and initialization details of the climate simulations. Section 3 presents a comparative assessment of simulated annual mean climate, and biases therein, between the simulations of CFSv2 and ESMv1. Section 4 describes the fidelity of simulated El Nino-Southern Oscillation (ENSO) and Pacific Decadal Oscillation (PDO), dominant modes of climate variability on interannual and decadal scales, and teleconnection of ENSO to ISM. The results are summarized in Section 5.

2. Brief Description of the IITM-ESMv1

The IITM-ESMv1 has been developed by replacing the ocean component Modular Ocean Model [MOM4p0, (Griffies et al. 2004)] of the CFSv2, by MOM4p1 (Griffies et al. 2009) retaining the land and atmospheric components.. The MOM4p1 has a better physics compared to MOM4p0, and also an interactive ocean bio-geochemistry (BGC) component (Dunne et al. 2012). The major differences between the ocean components of IITM-ESMv1 and CFSv2 are summarized in Annex-I.

Ocean and sea-ice components

The ocean component (MOM4p1) in IITM-ESMv1 is a hydrostatic model using Boussinesq approximation, and has a rescaled geopotential vertical coordinate (Stacey et al. 1995; Adcroft and Campin 2004) for a more robust treatment of free surface undulations. Key physical parameterizations include a KPP surface boundary layer scheme of (Large et al. 1994), which computes vertical diffusivity, vertical viscosity and non-local transport as a function of the flow and surface forcing. Griffies et al (2009) provide a detailed description about the model equation, physics, dynamics, time stepping schemes, and further subgrid scale parameterizations.

The IITM-ESMv1 ocean model has 40 vertical levels from surface to 4500 m, identical to that of the CFSv2. It has 27 levels in the upper 400m of water column in an attempt to capture surface boundary layer processes. Bottom topography is represented by the partial cell method described by (Adcroft et al. 1997) and (Pacanowski and Gnanadesikan 1998). Both the ocean and sea ice models use the Arakawa B-grid (Arakawa and Lamb 1977). The zonal resolution is 0.5° and the meridional resolution is 0.25° between 10°S and 10°N, becoming gradually coarser through the tropics, up to 0.5° poleward of 30°S and 30°N. The use of the (Murray 1996) bipolar grid facilitates removal of the coordinate singularity from the Arctic Ocean domain.

The sea ice component of IITM-ESMv1 is the GFDL Sea Ice Simulator (SIS) (Delworth et al. 2006; Winton 2000), which is an interactive dynamical sea ice model with three vertical layers, one snow and two ice, and five ice thickness categories.

Atmosphere and land components

The atmospheric component of IITM-ESMv1 is based on the NCEP GFS model, and has a spectral triangular truncation of 126 waves (T126) in the horizontal (~0.9° grid) and a finite differencing in the vertical with 64 sigma-pressure hybrid layers. It employs the Simplified Arakawa-Schubert convection scheme, with cumulus momentum mixing. The land surface model is the Noah LSM, with 4 layers (Ek et al. 2003, p. 200), same as in CFSv2. Further details can be availed in (Saha et al. 2010).

Coupling and initialization

The component models pass fluxes across their interfaces through an exchange grid system, which enforces the conservation of energy, mass and tracers. The atmosphere, land, and sea ice exchange quantities such as, heat and momentum fluxes every 10 minutes, with no flux adjustment or correction. The ocean tracer and atmosphere-ocean coupling time step is 30 minutes. The individual model components were initialized with 1 December, 2009 initial conditions derived from the NCEP CFS Reanalysis. The model has been integrated forward for a 100-year period without any changes in radiative forcing. Importantly, the biogeochemistry and ecosystem modules were switched off to facilitate a comparison of the simulated climate statistics with those from the CFSv2. For convenience, we refer to this simulation as the ESMv1 run. For comparison, we utilize the results from a 100 year run we carried out earlier with the CFSv2, which also started with the same initial conditions. Unless specified, the last 50-years of the simulations from both models are used for the comparison.

Observation-based datasets used for evaluating the simulations

For the evaluation of the model simulations, we use the SST data from World Ocean Atlas (WOA, 2009, Locarnini et al. 2010) and a density-based mixed layer depth data (de Boyer Montégut et al. 2004). We also use the HadISST1.1 dataset (Rayner et al. 2003), gridded rainfall data from IMD (Rajeevan et al. 2006) for the period 1930-2010 and gridded monthly rainfall data based on the TRMM Microwave Imager (TMI; Huffman et al. 2007) for 1998-2012, the NCEP and National Center for Atmospheric Research (NCEP/NCAR) reanalysis (Kalnay et al. 1996) circulation fields for the period 1980-2010. Global surface air temperature anomalies are obtained from NASA (Hansen et al. 2006), for the period of 2000 to 2010 and sea ice concentration data from HadISST (Rayner et al. 2003) for the period 1950-2010 is also utilized for the study.

The climatology for the ESMv1, and that for the CFSv2 are computed for the last 50 years of simulation. The simulated biases for any variable are computed by subtracting the observed value from the corresponding simulated value. The statistical significance of the bias is estimated based on 2-tailed Student's t-test.

3. Mean state in ESMv1

Annual mean surface temperature and SST

The time evolution of the global mean annual mean surface temperature and SST using ESMv1 and CFSv2 are examined (Figure 1). During the initial 30 years of the 100-year run, the

CFSv2 simulations undergo a rapid cooling from a global mean surface temperature (T_s) of 14.4 ^{o}C to 13^{o}C (Figure 1a), around which it lingers thereafter. This value is substantially less than the observed global T_s of 14.6 ^{o}C (Hansen et al. 2006), indicating a bias of at least 1.6 ^{o}C in the simulated global surface temperature. However, the initial cooling of simulated T_s by the ESMv1 is nearly about 0.6 ^{o}C (Figure 1a), and the T_s remains around 14.2 ^{o}C thereafter. Importantly, the drift in the SST simulated by the ESMv1, averaged globally or in tropics, is only about 0.4 ^{o}C, as compared to an SST bias of 1.4°C in CFSv2 (Figures1b & 1c).

The spatial map of the annual mean SST bias (Figure 2) indicates that the ESMv1 captures observed features well, at par with several other state-of-art coupled models (Figure not shown). The spatial map of SST bias, computed as the difference between the observed annual mean SST from that of the HadISST and over the last 50 years of simulations is shown for ESMv1 and CFSv2 in Figures 2b and 2c respectively. The 10% level of statistical significance of the SST bias estimated based on student's t-test are shown as contours in Figure 2. The results confirm a significant reduction in cold bias in the tropics between 30^{o}S to 30^{o}N, also as evidenced by the RMSE of 0.79 and 0.89 for the ESMv1and CFSv2, respectively. A similar reduction of the biases is seen in northern subtropical gyres. One of the potential reason for the better reduction of cold bias in the regions of northern subtropical gyres in ESMv1 is the use of the parameterization for the effect of sub-mesoscale mixed layer eddies (Fox-Kemper et al. 2011), which avoids mixed layer depths becoming excessively deep (Hallberg 2003); Figure 4a, and discussion in the following section). The improvements in ESMv1 have been further ascertained by comparing the simulations with the WOA (Figures not shown).

In both the models, particularly CFSv2, however, the cold bias lingers in the North Atlantic Current east of Newfoundland, which is a region of very sharp gradients in SST. Small errors in the paths of ocean boundary currents can lead to such large SST biases (Griffies et al. 2011). While there is a notable and a general improvement in the tropical SST simulation, the warm bias in the far-eastern Pacific cold tongue, and in the Southern Ocean has increased. We also note that warm biases are found in the Southern Ocean and in the upwelling region off the western coast of South America (Fig. 2b and 2c) in both the models, particularly in the ESMv1. The simulated warm bias in the southern ocean in ESMv1 is higher compared to CFSv2 and is due to the weaker-than-observed simulated lower level zonal winds (Figure not shown). A re-computation of the SST biases, after removing the mean global SST (Figure not shown) indicate that the difference between ESMv1 and CFSv2 is mainly reflected in the mean, and the spatial patterns of both ESMv1 and CFSv2 are nearly the same, with a significantly high pattern correlation (r=0.9), implying that the large scale features in both the models remains the same. e We note that most of the CMIP5 models exhibit similar biases with weaker-than-observed zonal winds in the southern ocean region (e.g. Fig. 5, Lee and Wang 2014)

Mean precipitation

The distributions of boreal summer monsoon (June-September) precipitation bias from ESMv1 and CFSv2 are shown in Figure 3. The 10% level of statistical significance of the precipitation bias estimated based on student's t-test are shown as contours in Figure 3. Both CFSv2 and ESMv1 models reproduce observed precipitation patterns reasonably well, though they show larger-than-observed precipitation in the tropical western and eastern Pacific and the South Pacific convergence zone. However, there is improvement in the oceanic precipitation in

ESMv1 in comparison with CFSv2, with a reduction of excess oceanic precipitation over the equatorial Maritime Continent region, eastern equatorial Indian Ocean and western tropical Pacific Ocean as compared to CFSv2.

Notwithstanding the improved SST in the tropical and northern Indian Ocean, the ESMv1 simulation also depicts a dry bias over India (Figure 3b). In terms of interannual variability of the ISMR, the ESMv1 shows a climatological precipitation rate of 4.3 mm.day^{-1} with a standard deviation of 0.53 mm.day^{-1} giving a coefficient of variation (the variability in relation to the observed mean) of 9%. The corresponding statistics for the observations are 6 mm.day^{-1}, 0.48 mm.day^{-1} and 8%, respectively. These results suggest a moderate improvement in the interannual variability of the land precipitation with respect to CFSv2, for which corresponding values are 4 mm.day^{-1}, 0.5 mm.day^{-1} and 7.5%, respectively. The ESMv1 also shows slight improvement in terms of intensity and propagation characteristics of monsoon intra-seasonal oscillation (figure not shown).

Ocean mixed layer and subsurface characteristics

One major difference between the ESMv1 and CFSv2 is that the former employs the scheme (Simmons et al. 2004) for interior mixing along with mixed layer re-stratification by the sub-mesoscale eddies (Fox-Kemper et al. 2008, 2011), as compared to the prescribed vertical diffusivity (Bryan and Lewis 1979) in the latter. To diagnose the role of such differences, we compare the simulated bias in annual mean ocean mixed layer depth (MLD) with respect to observations (Figure 4).

In general, the bias in the annual mean MLD is larger for CFSv2 (Figures 4b) compared to ESMv1 (Figure 4a). Significant improvement is seen in the tropical oceans especially in the

Arabian Sea and Bay of Bengal in ESMv1 simulations. The 10% level of statistical significance of the MLD bias estimated based on student's t-test are shown as contours in Figure 4. Notably, Roxy et al. (2012) found that large biases of MLD in CFSv2 in the Arabian Sea during the summer monsoon season lead to an exaggerated SST-precipitation relationship. Indeed, improvements in the ESMv1 simulated MLD and SST also reflect an improvement of precipitation in the tropics (Fig. 3). We however, note a deeper-than-observed MLD in the region of northern subtropical gyres, and shoaling in the southern ocean in simulations by both models (Fig. 4a and 4b). The southern ocean shoaling is relatively larger in ESMv1 simulation, and consistent with the warm SST bias over the region (Fig. 2b). Our sub-surface analysis shows that the warmer temperatures extend deeper in CFSv2 than WOA, and ESMv1, as shown by the position of the 4°C isotherm in the zonally-averaged vertical profiles of temperature (Figure 4c-e). This is also seen in all the three major individual ocean basins (Figure S1). This implies that pumping of heat away from the surface into deeper layers of the ocean takes place in the CFSv2, resulting in the cooling of surface and warming the ocean below.

4. Dominant Pacific modes of variability and interactions with Indian summer monsoon

The Pacific Ocean exhibits substantial temporal and spatial variability. The large size of the basin facilitates unique atmosphere-ocean interannual coupled variability in the tropics, which manifests as the El Niño/Southern Oscillation (ENSO; Rasmusson and Carpenter 1983). ENSO affects global climate and weather conditions such as droughts, floods (Ropelewski and Halpert 1987; Trenberth et al. 1998; Wallace et al. 1998; Ashok et al. 2007) and has significant impact on the Asian summer monsoon (Sikka 1980; Webster et al. 1998; Wallace et al. 1998; Kumar et al. 1999; Krishnamurthy and Goswami 2000; Lau et al. 2000; Ashok et al. 2004;

Shukla 1995; Keshavamurty 1982). In this section, we evaluate the fidelity of the simulated ENSO and its interaction with Indian summer monsoon. We also focus our attention on the fidelity of the simulated Pacific Decadal Oscillation (PDO). We use the last 75 years of ESMv1 and CFSv2 simulations, and qualitatively compared them with statistics from the 75 years (1935-2010) of HadISST data.

El Niño/Southern Oscillation (ENSO)

The largest observed SST variability (Figure 5a) is localized across the central-eastern equatorial Pacific, and is predominantly associated with the canonical ENSO. The models qualitatively reproduce the basic pattern of the observed SST anomaly variability. The coefficient of variation (contours) in Figure 5 indicates that the interannual variability is about 5% of the mean in observation and is well captured in ESMv1. However, the simulated variance in CFSv2 is significantly weaker as (Figure 5c) compared to the observations. The ESMv1, on the other hand, performs better both in terms of the magnitude and the extension of the variance maxima from the east through the dateline in the equatorial Pacific (figure 5b). In the CFSv2 simulations, the maximum variance is confined mostly to the eastern portion of the eastern equatorial Pacific. This is consistent with slightly flattened thermocline slope from central to eastern equatorial Pacific in CFSv2 compared to ESMv1 (Fig 5d). However, it is to be noted that the EMSv1 slightly overestimates the westward extension of the variance in comparison with observations and CFSv2. The thermocline is also relatively shallow in the west and deeper in the east for ESMv1, showing less improvement with respect to CFSv2.

In order to illustrate the fidelity of the spatial pattern of inter-annual variability associated with ENSO, the gravest EOF pattern for boreal winter (December-February) SST anomalies over the Pacific from the HadISST data and that from two models are presented in Figure 6. The horseshoe pattern in the Pacific associated with the observed ENSO variability, with unipolar loadings in the central and eastern equatorial Pacific, and oppositely signed loadings west of the dateline (Fig. 6a) is qualitatively captured by both the models (Figures 6b and 6c). The 31.5% variance explained by the EOF1 from the ESMv1 is reasonably close to corresponding value of 37% from the observations. The corresponding explained variance from the CFSv2 is slightly smaller, at 29.5%.

The time-mean global wavelet spectrum from a wavelet analysis on the observed PC1, which is associated with ENSO, shows a broad peak in the range of 2–7 years, with maximum power at ~5 years (Fig. 7d). Both models capture this broad peak reasonably well (Figures 7e & 7f). The ESMv1 also exhibits a decadal modulation of interannual variability (Figure 7b, 7e), similar to the observations (Figure 7a). Though longer time series are required to adequately characterize the ENSO (Wittenberg 2009), many of the simulated ENSO events appear to be episodic, spanning a range of frequencies over the course of one or two events.

ENSO-monsoon relationship in the coupled simulations

The ENSO-monsoon teleconnection, to a good extent, depends on the Walker circulation to deliver the Pacific SST signal to the Indian Ocean and Indian land sector (Krishnamurti 1971; Shukla and Paolino 1983; Webster and Yang 1992). Hence, for a better representation of the Indian summer monsoon and its variability, a model should adequately reproduce the spatial, seasonal, interannual and decadal aspects of the ENSO–monsoon connection.

We next compare the simulated ENSO-monsoon teleconnection in the climate simulations of ESMv1 and CFSv2 with one another, and also with that from observations. Figure 8 shows the lead–lag correlation between the ISMR and the monthly Niño-3.4 index. This will give a general idea on the mean ENSO-monsoon relationship, though it may not hold for its inter-decadal variability as the teleconnection changes on decadal time scales (eg: Krishnamurthy and Goswami 2000, Kriplani and Kulkarni 1998). The observed simultaneous negative correlation (Shukla and Paolino 1983) between Niño-3.4 SST and ISMR, along with the peak correlation after the monsoon, is reasonably simulated by the ESMv1. However, in CFSv2 simulations, the negative correlations unrealistically start developing 12 months prior to the monsoon season. Further, the correlation peaks just at the beginning of the monsoon season, 2-3 months earlier than observed. In fact, this is a common problem among most of the climate models, including a significant number of CMIP3 and CMIP5 models (Jourdain et al. 2013; Achuthavarier et al. 2012).

To understand the spatial variability of rainfall associated with ENSO, we project the summer monsoon rainfall onto the PC1 obtained from the EOF analysis (Figure 6) of the SST anomalies. The regression pattern from both the simulations show (Supplemental Figures S2) below normal rainfall over most the Indian region, with an excess of rainfall over northeast India similar to the observed pattern (Figure not shown) depicting the role of ENSO on Indian summer monsoon.

Pacific Decadal Oscillation (PDO)

The PDO is the dominant mode of inter-decadal variability in the Pacific characterized by warm SST anomalies near the equator and along the coast of North America, and cool SST anomalies in the central North Pacific in its positive phase (Mantua et al. 1997; Zhang et al. 1997; Power et al. 1999). Studies have shown that the PDO-related interdecadal variability can modulate the ENSO (Wang 1995) and the ENSO-related interannual variabilities. The PDO, with a periodicity of 20-30 years is shown to have significant impact on the climate around the Pacific Ocean and beyond (Krishnan and Sugi 2003; Power et al. 1999).

Following Mantua et al. (1997) we have performed an EOF analysis of detrended monthly SST anomalies over the domain 120E-120W; 20N-60N for the last 75 years of simulations to explore the simulated the PDO signal. For comparison, an EOF analysis is also performed on HadISST data for the period 1935-2010 over the same domain. The EOF1 from the model and observations are shown in Figures 9. EOF1 pattern from HadISST data, explains about 30.3% variance, with a unipolar signal in the central North Pacific surrounded by the oppositely phased loadings hugging along the west coast of North America (Fig. 9a). This is the distinguishing feature of the warm phase of PDO (e.g. Fig.1, Krishnamurthy and Krishnamurthy 2013). The corresponding EOF1 from the ESMv1 (Fig9b) captures the pattern and associated explained variance reasonably. On the other hand, the analogous EOF1 for the CFSv2 (Fig 9c) explains only 24.4% of total variance, and the spatial pattern shows relatively weak negative loadings in the north Pacific. This may be associated with the strong cold SST bias in the subtropical Pacific.

A wavelet power spectrum analysis on the observed PC1 (Fig. 9) indicates a dominant, and statistically significant, power in the band of 16-32 years (Figures 10a and 10d). The ESMv1 successfully reproduces this dominant peak (Figures 10b and 10e). However, in the CFSv2 simulations, it is weaker and not statistically significant (Figure 10c and 10f).

Further, a regression of the December-February surface winds on to the PC1 indicates an enhanced counterclockwise wind stress anomalies over the North Pacific (Supplemental Fig. S3a) associated with the PDO. Such an association is also seen in the simulations from the ESMv1 (Fig. S3b). The location of the anticyclonic winds and their magnitude are well simulated. However, the counter-clockwise surface circulation is weaker in CFSv2 simulations (Fig. S3c) as compared to observation and ESMv1 simulation. These, along with weaker-than-observed westerlies over subtropical Pacific and south-easterlies over North American coast are consistent with a weak PDO signal.

PDO and Indian Summer Monsoon

Krishnan and Sugi (2003) suggest that a warm phase of PDO can amplify the impact of El Niño, resulting in the weakening of Indian summer monsoon. Krishnamurthy and Krishnamurthy (2013) have shown that the PDO is associated with deficit rainfall anomalies mainly north of 18°N, with stronger anomalies in the eastern central India. Indeed, a regression of the observed boreal summer monsoon rainfall (Rajeevan et al. 2006), for the period 1935-2010 on to the concurrent PDO index from the HadISST (Fig. 11a) conforms to these earlier observational works. The corresponding results from the simulations, (Figures 11b and 11c) are in qualitative agreement with Fig. 11a. However, the regression pattern from the CFSv2 simulation shows a slightly weaker-than-observed signal.

5. Summary and Conclusion

This paper documents the development of the first prototype of the IITM Earth System Model (ESMv1). Derived from the NCEP CFSv2, this model is being developed to be used in studies on the detection, attribution, and projections of climate change and its impact on the South Asian region. The effort particularly involved, as a first step towards the development of the IITM ESM, inclusion of an ocean bio-geochemistry and ecosystem module and improved physics by replacing the ocean component of the CFSv2. 100-year simulations were performed with the ESMv1and CFSv2, using the same initial conditions, and compared. The new ocean formulation has led to a significant reduction of cold atmospheric temperature bias (from 1.5ºC to 0.6ºC) and SST bias as compared to that in the CFSv2. The improvement in SST is particularly prominent in the tropical Indian and Pacific oceans. As a result, the precipitation over the tropical oceans has also improved considerably.

In addition, the simulations with IITM-ESMv1 also show improvements in the mean state and near-surface biases in the northern subtropical gyres as well, implying the role of ocean physics in the coupled climate simulations. Importantly, the model demonstrates a realistic global mean temperature and reasonable sensitivity to the ambient CO_2, an essential pre-requisite for a climate model to be used for climate change studies.

In terms of the spatial pattern and the periodicity, the ESMv1 simulations of climate variability are more realistic as compared to those of NCEP CFSv2. An example is the simulated PDO signal in CFSv2, which is much weaker than that observed. Importantly, the ENSO-Monsoon relationship in CFSv2 shows an unrealistic strong, negative correlation maximum between the Indian summer Monsoon rainfall and Niño-3.4 index 6-9 months prior to the observations, which may result in unrealistic monsoon variations. This is a common problem in many of the CMIP5 models (Jourdain et al. 2013). However, the ESMv1 captures the observed concurrent negative simultaneous correlations between the monsoons and ENSO, as well as a reasonable lead-lag relationship between these two. All these features demonstrate the ability of the ESMv1 to capture the crucial monsoon-ENSO links, which are important in manifesting the interannual variability of the South Asian summer monsoon. A companion study (Shikha et al. 2014) also demonstrates that the ESMv1 also simulates a realistic evolution of the Indian Ocean Dipole (Saji et al. 1999; Webster et al. 1999; Murtugudde 2000) and its variability (figure not shown).

A preliminary analysis of the simulated Atlantic Meridional Overturning Circulation (AMOC) indicates (Figure not shown), that the full AMOC has not been yet established in the simulation, and warrants the extension of the current integration by a few more hundreds of years. Such a longer run will also result in more robust tropical climate statistics (e.g. Wittenberg 2009) We have also analyzed the distribution of sea-ice concentration (Figure S4) in the northern hemisphere from ESMv1 and CFSv2 for January-March (JFM) and June-September (JJAS). The northern hemisphere sea-ice concentration in ESMv1 is comparable with HadISST data during JFM, the season when the sea ice coverage is largest in the northern hemisphere, but it is found to be lower than observations during boreal summer season (JJAS). Further, the southern hemisphere sea ice concentration is lower than observed (Figure not sown) and more or less similar to that of the CFSv2. Importantly, Huang et al. (2014) note that the low sea ice concentration in CFSv2 has led to a weaker-than-observed AMOC in CFSv2, and improvement in sea ice concentration can be achieved by improving the sea ice albedo. Therefore, we plan to improve the sea ice parameters and also the coupling according to Huang et al. (2014) and extend the integration further to study the relevance of AMOC changes for the monsoon variability.

The model's fidelity in terms of the mean climate and seasonal cycle simulations, are at par with those of some other state of art models, the model has yet a few limitations such as a warm bias in the southern ocean region, which are common across a wide spectrum of the CMIP5 models (Lee and Wang 2014). Another important issue is that the CFSv2 has a top of the atmosphere energy imbalance of $6Wm^{-2}$, which is fairly constant over a 100-year simulation (figure not shown). A similar signal is also associated with ESMv1. Since the temperature has stabilized, the imbalance could be due to some unaccountable source of energy that is not tracked as part of model integration, for example, due to the lack of dissipative heating of the turbulent kinetic energy (TKE, e.g. Fiedler 2007), or neglecting the radiative impact of precipitating hydrometeors (Waliser et al. 2011). Sun et al (2010), Huang et al. (2007) and Hu et al. (2008) have pointed out that CFS has low cloud cover, this may be one of the possible reasons for the top of the atmosphere energy imbalance in ESMv1. In this context, it is worth noting that the annual average absorbed shortwave and outgoing long wave radiation across the ITCZ regions for the ensemble average of CMIP3 GCMs were shown biases as reported by Trenberth and Fasullo (2010). Trenberth and Fasullo (2010) also find that many of the CMIP3 models poorly simulate the energy budget in the southern hemisphere. This aspect needs further attention. Importantly, a recent study by Bombardi et al. (2014) shows that, despite such biases, retrospective decadal forecasts by the CFSv2 model show high predictive skill over the Indian, the western Pacific, and the Atlantic Oceans. Another issue that needs further attention is that despite an improvement in the oceanic precipitation, the dry bias over the Indian subcontinent associated with the CFSv2 simulations is still seen in the ESMv1 simulations as well. These issues will be addressed in the next version of the model. Significantly, a few recent sensitivity experiments carried out using the CFSv2 model (Hazra et al. 2014) suggest that improving the cloud microphysics will alleviate this problem substantially. In addition, parallel efforts are also towards including an aerosol module into the ESM.

Summing up, the ESMv1 is a promising development to facilitate future projections relevant to South Asian climate, specifically those that envisage the next 3-5 decades horizon.

Acknowledgements:

We thank the Editor Dr. Brian Etherton for conducting the review process and three anonymous reviewers for the constructive comments. The authors acknowledge Drs. S. M. Griffies, V. Balaji, Xingren Wu and R. Murtugudde for technical discussions, and Ms. B. Preethi for her help in making CFSv2 simulations. The IITM including CCCR is part of the Ministry of Earth Sciences, Government of India.

References

Achuthavarier, D., and V. Krishnamurthy, 2010: Relation between intraseasonal and interannual variability of the South Asian monsoon in the National Centers for Environmental Predictions forecast systems. *J. Geophys. Res.*, **115**, D08104, doi:10.1029/2009JD012865.

Achuthavarier, D., V. Krishnamurthy, B. P. Kirtman, and B. Huang, 2012: Role of the Indian Ocean in the ENSO–Indian Summer Monsoon Teleconnection in the NCEP Climate Forecast System. *J. Clim.*, **25**, 2490–2508, doi:10.1175/JCLI-D-11-00111.1.

Adcroft, A., and J. M. Campin, 2004: Rescaled height coordinates for accurate representation of free-surface flows in ocean circulation models. *Ocean Model.*, **7**, 269–284, doi:10.1016/j.ocemod.2003.09.003.

Adcroft, A., C. Hill, and J. Marshall, 1997: Representation of Topography by Shaved Cells in a Height Coordinate Ocean Model. *Mon. Weather Rev.*, **125**, 2293–2315, doi:10.1175/1520-0493(1997)125<2293:ROTBSC>2.0.CO;2.

Arakawa, A., and V. R. Lamb, 1977: Computational design of the basic dynamical processes of the UCLA general circulation model. *Methods Comput. Phys.*, **17**, 173–265.

Ashok, K., Z. Guan, N. H. Saji, and T. Yamagata, 2004: Individual and Combined Influences of ENSO and the Indian Ocean Dipole on the Indian Summer Monsoon. *J. Clim.*, **17**, 3141–3155, doi:10.1175/1520-0442(2004)017<3141:IACIOE>2.0.CO;2.

Ashok, K., S. K. Behera, S. a. Rao, H. Weng, and T. Yamagata, 2007: El Niño Modoki and its possible teleconnection. *J. Geophys. Res.*, **112**, C11007, doi:10.1029/2006JC003798.

Bombardi, R. J. and Coauthors, 2014: Evaluation of the CFSv2 CMIP5 Decadal Predictions. *Clim. Dyn.*, Under revision.

De Boyer Montégut, C., G. Madec, A. S. Fischer, A. Lazar, and D. Iudicone, 2004: Mixed layer depth over the global ocean: An examination of profile data and a profile-based climatology. *J Geophys Res*, **109**, C12003.

Bryan, K., and L. J. Lewis, 1979: A water mass model of the World Ocean. *J. Geophys. Res.*, **84**, 2503, doi:10.1029/JC084iC05p02503.

Chaudhari, H. S. and Coauthors, 2013: Model biases in long coupled runs of NCEP CFS in the context of Indian summer monsoon. *Int. J. Climatol.*, **33**, 1057–1069, doi:10.1002/joc.3489.

Delworth, T. L. and Coauthors, 2006: GFDL's CM2 Global Coupled Climate Models. Part I: Formulation and Simulation Characteristics. *J. Clim.*, **19**, 643–674.

Delworth, T. L. and Coauthors, 2012: Simulated Climate and Climate Change in the GFDL CM2.5 High-Resolution Coupled Climate Model. *J. Clim.*, **25**, 2755–2781, doi:10.1175/JCLI-D-11-00316.1.

Dunne, J. P. and Coauthors, 2012: GFDL's ESM2 Global Coupled Climate–Carbon Earth System Models. Part I: Physical Formulation and Baseline Simulation Characteristics. *J. Clim.*, **25**, 6646–6665, doi:10.1175/JCLI-D-11-00560.1.

Ek, M. B., K. E. Mitchell, Y. Lin, E. Rogers, P. Grunmann, V. Koren, G. Gayno, and J. D. Tarpley, 2003: Implementation of Noah land surface model advances in the National Centers for Environmental Prediction operational mesoscale Eta model. *J Geophys Res*, **108**, 8851, doi:10.1029/2002JD003296.

Fiedler, B. H., 2007: Dissipative heating in climate models. *Q. J. R. Meteorol. Soc.*, **126**, 925–939, doi:10.1002/qj.49712656408.

Fox-Kemper, B., R. Ferrari, and R. Hallberg, 2008: Parameterization of Mixed Layer Eddies. Part I: Theory and Diagnosis. *J. Phys. Oceanogr.*, **38**, 1145–1165.

Fox-Kemper, B. and Coauthors, 2011: Parameterization of mixed layer eddies. III: Implementation and impact in global ocean climate simulations. *Ocean Model.*, **39**, 61–78, doi:10.1016/j.ocemod.2010.09.002.

Griffies, S., M. Schmidt, and M. Herzfeld, 2009: Elements of mom4p1. *GFDL Ocean Group Tech Rep*,.

Griffies, S. M., M. J. Harrison, R. C. Pacanowski, and A. Rosati, 2004: A technical guide to MOM4. *GFDL Ocean Group Tech Rep*, **5**, 371.

Hallberg, R. W., 2003: The suitability of large-scale ocean models for adapting parameterizations of boundary mixing and a description of a refined bulk mixed layer model. *Near-Boundary Processes and Their Parameterization, Proceedings of the 13th "Aha Huliko" a Hawaiian Winter Workshop*, 187–203.

Hansen, J., M. Sato, R. Ruedy, K. Lo, D. W. Lea, and M. Medina-Elizade, 2006: Global temperature change. *Proc. Natl. Acad. Sci.*, **103**, 14288–14293.

Hazra, A., H. S. Chaudhari, S. A. Rao, B. N. Goswami, A. Dhakate, S. Pokhrel, and S. K. Saha, 2014: Improvement in Indian Summer Monsoon simulations for NCEP CFSv2 through modification of cloud microphysical scheme and critical humidity. *Under preparation*.

Huang, B., Z.-Z. Hu, and B. Jha, 2007: Evolution of model systematic errors in the tropical Atlantic basin from the NCEP coupled hindcasts. *Clim. Dyn.,* **28***,* 661–682*,* doi:10.1007/s00382-006-0223-8.

Huang. B., et al. and co-authors, 2014: Climate drift of AMOC, north Atlantic salinity and Arctic sea ice in CFSv2 decadal predictions. *Clim. Dyn*., submitted.

Hu Z-Z., B. Huang, and K. Pegion, 2008: Low cloud errors over the southeastern Atlantic in the NCEP CFS and their association with lower-tropospheric stability and air- sea interaction. *J. Geophysc. Res.*, **113**, doiI: 10.1029/2007JD009514.

Huffman, G. J. and Coauthors, 2007: The TRMM Multisatellite Precipitation Analysis (TMPA): Quasi-Global, Multiyear, Combined-Sensor Precipitation Estimates at Fine Scales. *J. Hydrometeorol.*, **8**, 38–55, doi:10.1175/JHM560.1.

Hu, Z.-Z., A. Kumar, B. Huang, W. Wang, J. Zhu, and C. Wen, 2012: Prediction skill of monthly SST in the North Atlantic Ocean in NCEP Climate Forecast System version 2. *Clim. Dyn.*, **40**, 2745–2759, doi:10.1007/s00382-012-1431-z.

Jiang, X., S. Yang, Y. Li, A. Kumar, X. Liu, Z. Zuo, and B. Jha, 2013: Seasonal-to-Interannual Prediction of the Asian Summer Monsoon in the NCEP Climate Forecast System Version 2. *J. Clim.*, **26**, 3708–3727, doi:10.1175/JCLI-D-12-00437.1.

Jourdain, N. N., A. A. Gupta, A. Taschetto, C. Ummenhofer, A. Moise, and K. Ashok, 2013: The Indo-Australian monsoon and its relationship to ENSO and IOD in reanalysis data and the CMIP3/CMIP5 simulations. *Clim. Dyn.*, **41**, 3073–3102, doi:10.1007/s00382-013-1676-1.

Kalnay, E. and Coauthors, 1996: The NCEP/NCAR 40-Year Reanalysis Project. *Bull. Am. Meteorol. Soc.*, **77**, 437–471, doi:10.1175/1520-0477(1996)077<0437:TNYRP>2.0.CO;2.

Keshavamurty, R. N., 1982: Response of the atmosphere to sea surface temperature anomalies over the equatorial Pacific and the teleconnections of the Southern Oscillation. *J. Atmospheric Sci.*, **39**, 1241–1259.

Kripalani, R. H., and K. Ashwini Kulkarni, 1998: The relationship between some large scale atmospheric parameters and Rainfall over Southeast Asia : A comparison with features over India. *Theor. Appl. Climatol.*, 59, 1-11.

Krishnamurthy, L., and V. Krishnamurthy, 2013: Influence of PDO on South Asian summer monsoon and monsoon–ENSO relation. *Clim. Dyn.*, 1–14, doi:10.1007/s00382-013-1856-z.

Krishnamurthy, V., and B. Goswami, 2000: Indian monsoon-ENSO relationship on interdecadal timescale. *J. Clim.*, **13**, 579–595.

Krishnamurti, T., 1971: Tropical east-west circulations during the northern summer. *J. Atmospheric Sci.*, **28**, 1342–1347.

Krishnan, R., and M. Sugi, 2003: Pacific decadal oscillation and variability of the Indian summer monsoon rainfall. *Clim. Dyn.*, **21**, 233–242.

Kumar, K. K., B. Rajagopalan, and M. A. Cane, 1999: On the weakening relationship between the Indian monsoon and ENSO. *Science*, **284**, 2156–2159.

Large, W., J. McWilliams, and S. Doney, 1994: Oceanic vertical mixing: A review and a model with a nonlocal boundary layer parameterization. *Rev. Geophys.*, **32**, 363–403.

Lau, N., M. Nath, Lau, and Nath, 2000: Impact of ENSO on the Variability of the Asian – Australian Monsoons as Simulated in GCM Experiments The relationships between the Asian – Australian monsoon. *J. Clim.*, 4287–4309.

Lee, J., and B. Wang, 2014: Future change of global monsoon in the CMIP5. *Clim. Dyn.*, **42**, 101–119.

Locarnini, R. A., A. V. Mishonov, J. I. Antonov, T. P. Boyer, and H. E. Garcia, 2010: *World Ocean Atlas 2009, Volume 1: Temperature. S. Levitus, Ed., NOAA Atlas NESDIS 68, U.S. Government Printing Office, Washington, D.C.,*. 184 pp.

Mantua, N. J., S. R. Hare, Y. Zhang, J. M. Wallace, and R. C. Francis, 1997: A Pacific Interdecadal Climate Oscillation with Impacts on Salmon Production. *Bull. Am. Meteorol. Soc.*, **78**, 1069–1079, doi:10.1175/1520-0477(1997)078<1069:APICOW>2.0.CO;2.

Murray, R. J., 1996: Explicit Generation of Orthogonal Grids for Ocean Models. *J. Comput. Phys.*, **126**, 251–273, doi:10.1006/jcph.1996.0136.

Murtugudde, R., 2000: Oceanic processes associated with anomalous events in the Indian Ocean with relevance to 1997–1998. *J. Geophys. Res.*, **105**, 3295.

Pacanowski, R. C., and A. Gnanadesikan, 1998: Transient Response in a Z -Level Ocean Model That Resolves Topography with Partial Cells. *Mon. Weather Rev.*, **126**, 3248–3270, doi:10.1175/1520-0493(1998)126<3248:TRIAZL>2.0.CO;2.

Pattanaik, D., and A. Kumar, 2010: Prediction of summer monsoon rainfall over India using the NCEP climate forecast system. *Clim. Dyn.*, **34**, 557–572.

Pokhrel, S., H. S. Chaudhari, S. K. Saha, A. Dhakate, R. K. Yadav, K. Salunke, S. Mahapatra, and S. A. Rao, 2012: ENSO, IOD and Indian Summer Monsoon in NCEP climate forecast system. *Clim. Dyn.*, **39**, 2143–2165, doi:10.1007/s00382-012-1349-5.

Pokhrel, S., A. Dhakate, H. S. Chaudhari, and S. K. Saha, 2013: Status of NCEP CFS vis-a-vis IPCC AR4 models for the simulation of Indian summer monsoon. *Theor. Appl. Climatol.*, **111**, 65–78, doi:10.1007/s00704-012-0652-8.

Power, S., T. Casey, C. Folland, A. Colman, and V. Mehta, 1999: Inter-decadal modulation of the impact of ENSO on Australia. *Clim. Dyn.*, **15**, 319–324, doi:10.1007/s003820050284.

Rajeevan, M., J. Bhate, J. D. Kale, and B. Lal, 2006: High resolution daily gridded rainfall data for the Indian region: Analysis of break and active monsoon spells. *Curr. Sci.*, **91**, 296–306.

Rasmusson, E. M., and T. H. Carpenter, 1983: The Relationship Between Eastern Equatorial Pacific Sea Surface Temperatures and Rainfall over India and Sri Lanka. *Mon. Weather Rev.*, **111**, 517–528, doi:10.1175/1520-0493(1983)111<0517:TRBEEP>2.0.CO;2.

Rayner, N. A., D. E. Parker, E. B. Horton, C. K. Folland, L. V. Alexander, D. P. Rowell, E. C. Kent, and A. Kaplan, 2003: Global analyses of sea surface temperature, sea ice, and night marine air temperature since the late nineteenth century. *J Geophys Res*, **108**, 4407, doi:10.1029/2002JD002670.

Ropelewski, C. F., and M. S. Halpert, 1987: Global and Regional Scale Precipitation Patterns Associated with the El Niño/Southern Oscillation. *Mon. Weather Rev.*, **115**, 1606–1626, doi:10.1175/1520-0493(1987)115<1606:GARSPP>2.0.CO;2.

Roxy, M., Y. Tanimoto, B. Preethi, P. Terray, and R. Krishnan, 2012: Intraseasonal SST-precipitation relationship and its spatial variability over the tropical summer monsoon region. *Clim. Dyn.*, **41**, 1–17, doi:10.1007/s00382-012-1547-1.

Saha, S. and Coauthors, 2006: The NCEP climate forecast system. *J. Clim.*, **19**, 3483–3517.

Saha, S. and Coauthors, 2010: The NCEP climate forecast system reanalysis. *Bull. Am. Meteorol. Soc.*, **91**, 1015–1057.

Saha, S. and Coauthors, 2013: The NCEP climate forecast system version 2. *J. Clim.*, **27**, 2185–2208, doi:10.1175/JCLI-D-12-00823.1.

Saji, N. H., B. N. Goswami, P. N. Vinayachandran, and T. Yamagata, 1999: A dipole mode in the tropical Indian Ocean. *Nature*, **401**, 360–363, doi:10.1038/43854.

Semtner, A. A. J., and R. R. M. Chervin, 1992: Ocean general circulation from a global eddy- resolving model. *J. Geophys. Res.*, **97**, 5493, doi:10.1029/92JC00095.

Shikha, S., V. Valsala, P. Swapna, and M. K. Roxy, 2014: Indian Ocean Dipole in CFSv2 & ESMv1: Role of ocean biases. *Under preparation*,.

Shukla, J., 1995: Predictability of the tropical atmosphere, the tropical ocean and TOGA. *Proc. Int. Conf. on the Tropical Ocean and Global Atmosphere (TOGA) Programme, Rep. WCRP-91*, Geneva, Switzerland, 725–730.

Shukla, J., and D. A. Paolino, 1983: The Southern Oscillation and long-range forecasting of the summer monsoon rainfall over India. *Mon. Weather Rev.*, **111**, 1830–1837, doi:10.1175/1520-0493(1983)111<1830:TSOALR>2.0.CO;2.

Sikka, D., 1980: Some aspects of the large scale fluctuations of summer monsoon rainfall over India in relation to fluctuations in the planetary and regional scale circulation parameters. *Proc. Indian Acad. Sci.-Earth Planet. Sci.*, **89**, 179–195.

Simmons, H. L., S. R. Jayne, L. C. S. Laurent, and A. J. Weaver, 2004: Tidally driven mixing in a numerical model of the ocean general circulation. *Ocean Model.*, **6**, 245–263, doi:10.1016/S1463-5003(03)00011-8.

Stacey, M. W. M., S. Pond, and Z. P. Z. Nowak, 1995: A Numerical Model of the Circulation in Knight Inlet, British Columbia, Canada. *J. Phys. Oceanogr.*, **25**, 1037–1062, doi:10.1175/1520-0485(1995)025<1037:ANMOTC>2.0.CO;2.

Sun, R., S. Moorthi, H. Xiao, and C. R. Mechoso, 2010: Simulation of low clouds in the south east Pacific by the NCEP GFS: sensitivity to vertical mixing. *Atmos. Chem. Phys.,* **10**, 12261-12272, doi:10.5194/acp-10-12261-2010.

Trenberth, K. E., and J. T. Fasullo, 2010: Simulation of Present-Day and Twenty-First-Century Energy Budgets of the Southern Oceans. *J. Clim.*, **23**, 440–454, doi:10.1175/2009JCLI3152.1.

Trenberth, K. E., G. G. W. Branstator, D. Karoly, A. Kumar, N.-C. Lau, and C. Ropelewski, 1998: Progress during TOGA in understanding and modeling global teleconnections associated with tropical sea surface temperatures. *J. Geophys. Res.*, **103**, 14,291–14,324, doi:10.1029/97JC01444.

Waliser, D. E., J.-L. F. Li, T. S. L'Ecuyer, and W.-T. Chen, 2011: The impact of precipitating ice and snow on the radiation balance in global climate models. *Geophys. Res. Lett.*, **38**, n/a–n/a, doi:10.1029/2010GL046478.

Wallace, J., E. Rasmusson, and T. Mitchell, 1998: On the structure and evolution of ENSO- related climate variability in the tropical Pacific: Lessons from TOGA. *J. Geophys. Res.*, **103**, 14241.

Wang, B., 1995: Interdecadal Changes in El Niño Onset in the Last Four Decades. *J. Clim.*, **8**, 267–285, doi:10.1175/1520-0442(1995)008<0267:ICIENO>2.0.CO;2.

Wang, W., S. Saha, H.-L. H. Pan, S. Nadiga, and G. White, 2005: Simulation of ENSO in the new NCEP coupled forecast system model (CFS03). *Mon. Weather Rev.*, **133**, 1574–1593, doi:10.1175/MWR2936.1.

Weaver, S., W. Wang, M. Chen, and A. Kumar, 2011: Representation of MJO variability in the NCEP Climate Forecast System. *J. Clim.*, **24**, 4676–4694.

Webster, P., V. Magana, and T. Palmer, 1998: Monsoons: Processes, predictability, and the prospects for prediction. *J. Geophys. Res.*, **103**, 14451.

Webster, P. J., A. M. Moore, J. P. Loschnigg, and R. R. Leben, 1999: Coupled ocean-atmosphere dynamics in the Indian Ocean during 1997-98. *Nature*, **401**, 356–360, doi:10.1038/43848.

Webster, P. P. J., and S. Yang, 1992: Monsoon and Enso: Selectively Interactive Systems. *Q. J. R. Meteorol. Soc.*, **118**, 877–926, doi:10.1002/qj.49711850705.

Winton, M., 2000: A reformulated three-layer sea ice model. *J. Atmospheric Ocean. Technol.*, **17**, 525–531, doi:10.1175/1520-0426(2000)017<0525:ARTLSI>2.0.CO;2.

Wittenberg, A. T., 2009: Are historical records sufficient to constrain ENSO simulations? *Geophys. Res. Lett.*, **36**, L12702, doi:10.1029/2009GL038710.

Yang, S., Z. Zhang, V. E. Kousky, R. W. Higgins, S.-H. Yoo, J. Liang, and Y. Fan, 2008: Simulations and Seasonal Prediction of the Asian Summer Monsoon in the NCEP Climate Forecast System. *J. Clim.*, **21**, 3755–3775, doi:10.1175/2008JCLI1961.1.

Yuan, X., E. E. F. E. Wood, L. Luo, and M. Pan, 2011: A first look at Climate Forecast System version 2 (CFSv2) for hydrological seasonal prediction. *Geophys. Res. Lett.*, **38**, n/a, doi:10.1029/2011GL047792.

Zhang, Q., A. Kumar, and Y. Xue, 2007: Analysis of the ENSO cycle in the NCEP coupled forecast model. *J. Clim.*, **20**, 1265–1284.

Zhang, Y., J. M. Wallace, and D. S. Battisti, 1997: ENSO-like Interdecadal Variability: 1900–93. *J. Clim.*, **10**, 1004–1020, doi:10.1175/1520-0442(1997)010<1004:ELIV>2.0.CO;2.

Figure Captions:

Figure 1. Time evolution of the globally-averaged annual mean fields (^{o}C) of (a) near surface temperature (b) sea surface temperature and (c) tropical sea surface temperature (30^{o}S-30^{o}N). The ESMv1 (CFSv2) simulations are in red (blue). The corresponding annual mean observational values are 14. 6 ^{o}C, 18.6 ^{o}C and 26.1 ^{o}C respectively

Figure 2. Spatial distribution of annual mean SST (^{o}C) from (a) HadISST and the bias for (b) ESMv1 and (c) CFSv2. The contours represent 10% level of statistical significance based on student's t-test. The rms errors for the ESMv1 are, 1.1 ^{o}C (global), 0.79^{o}C (30^{o}S-30^{o}N), and for CFSv2, 1.1^{o}C (global), 0.89^{o}C (30^{o}S-30^{o}N).

Figure 3. Spatial map of mean summer monsoon precipitation (JJAS; mm day^{-1}) from the (a) TRMM and the biases for (b) ESMv1 and (c) CFSv2. The contours represent 10% level of statistical significance based on student's t-test.

Figure 4a. Spatial maps of bias in annual mean mixed layer depth for ESMv1 and (b) CFSv2. The model results are computed over the last 50 years of simulation. Biases are in meter. The contours represent 10% level of statistical significance based on student's t-test. (c) vertical distribution of the global ocean zonal mean temperature (°C) from WOA (d) and (e) same as (c) except for ESMv1 and CFSv2 respectively.

Figure 5. Standard deviation of interannual SST anomalies (°C, shaded) for (a) HadISST (b) ESMv1 and (c) CFSv2. The coefficient of variation (%) are overlaid as contours. (d) depth of 20 ^{o}C isotherm (m) in the equatorial Pacific (5^{o}S-5^{o}N) for WOA, ESMv1 and CFS2

Figure 6. The leading EOF pattern of boreal winter (December-February) SST anomalies (°C) in the pacific for (a) HadISST data for the period 1935-2010 (b) ESMv1 and (c) CFSv2. The model results are computed over the last 75 years of simulations.

Figure 7. Time series of wavelet power spectra of the gravest principal component from the EOF analysis of the pacific winter SST (120^{o}E-80^{o}W,60^{o}N-60^{o}S; see Fig. 6) for (a) HadISST (b) ESMv1 and (c) CFSv2. The corresponding time-averaged power spectra are shown for (d) HadISST (e) ESMv1 and (f) CFSv2.

Figure 8. Lead–lag correlations between All Indian Summer Monsoon derived from the IMD datasets (June-September) rainfall and monthly Nino-3.4 index from the HadISST, for the 1935-2010 period (black line), ESMv1 (red line), CFSv2 (blue line). Note that the model results are computed over the last 75 years of simulations for comparison.

Figure 9. The leading EOF pattern of detrended monthly SST anomalies (°C) in the north Pacific (120^{o}E-120^{o}W, 20^{o}N-60^{o}N) (a) HadISST data for the period 1935-2010 (b) ESMv1 and (c) CFSv2. The model results are computed over the last 75 years of simulations.

Figure 10. Time series of wavelet power spectra of the gravest principal component from the EOF analysis of the northern pacific SST (120^{o}E-120^{o}W, 20^{o}N-60^{o}N; see Fig. 9) for (a) HadISST (b) ESMv1 (c) CFSv2 and the black contour is the 10% significance level. (d) the corresponding time-averaged spectra. The dashed line is the 10% significance for the time-averaged power spectra.

Figure 11. Spatial map of JJAS rainfall anomalies (mm day^{-1}) regressed on to the gravest principal component from EOF analysis of northern pacific (120^{o}E-120^{o}W, 20^{o}N-60^{o}N; see

Figure 9) from (a) Observations (for the period 1935-2010) (b) ESMv1 and (c) CFSv2. The model results are computed over the last 75 years of simulations.

Supplementary figures:

Figure S1. Vertical distribution of the global ocean zonal mean temperature (°C) for individual ocean basins (Pacific : top panel, Indian : middle panel and Atlantic : bottom panel) from (a) WOA (b) ESMv1 and (c) CFSv2.

Figure S2. Spatial map of JJAS rainfall anomalies (mm day^{-1}) regressed on to the gravest principal component from EOF analysis of the pacific SST (120^{o}E-80^{o}W, 60^{o}N-60^{o}S; see Figure 6) from (a) Observation (for the period 1935-2010) (b) ESMv1 and (c) CFSv2. The model results are computed over the last 75 years of simulation.

Figure S3. Spatial map of DJF surface wind anomalies (ms^{-1}) regressed on to the gravest principal component from EOF analysis of the Pacific SST (120^{o}E-120^{o}W, 20^{o}N-60^{o}N; see Figure 9) from upon the wind anomalies from (a) Observation (NCEP reanalysis) (b) ESMv1 and (c) CFSv2.

Figure S4. Sea ice concentration in the northern hemisphere north of 60^{o}N during January-March (JFM) from (a) HadISST (b) ESMv1 and (c) CFSv2, (d) –(e) same as (a)-(c) except during June-August (JJA).

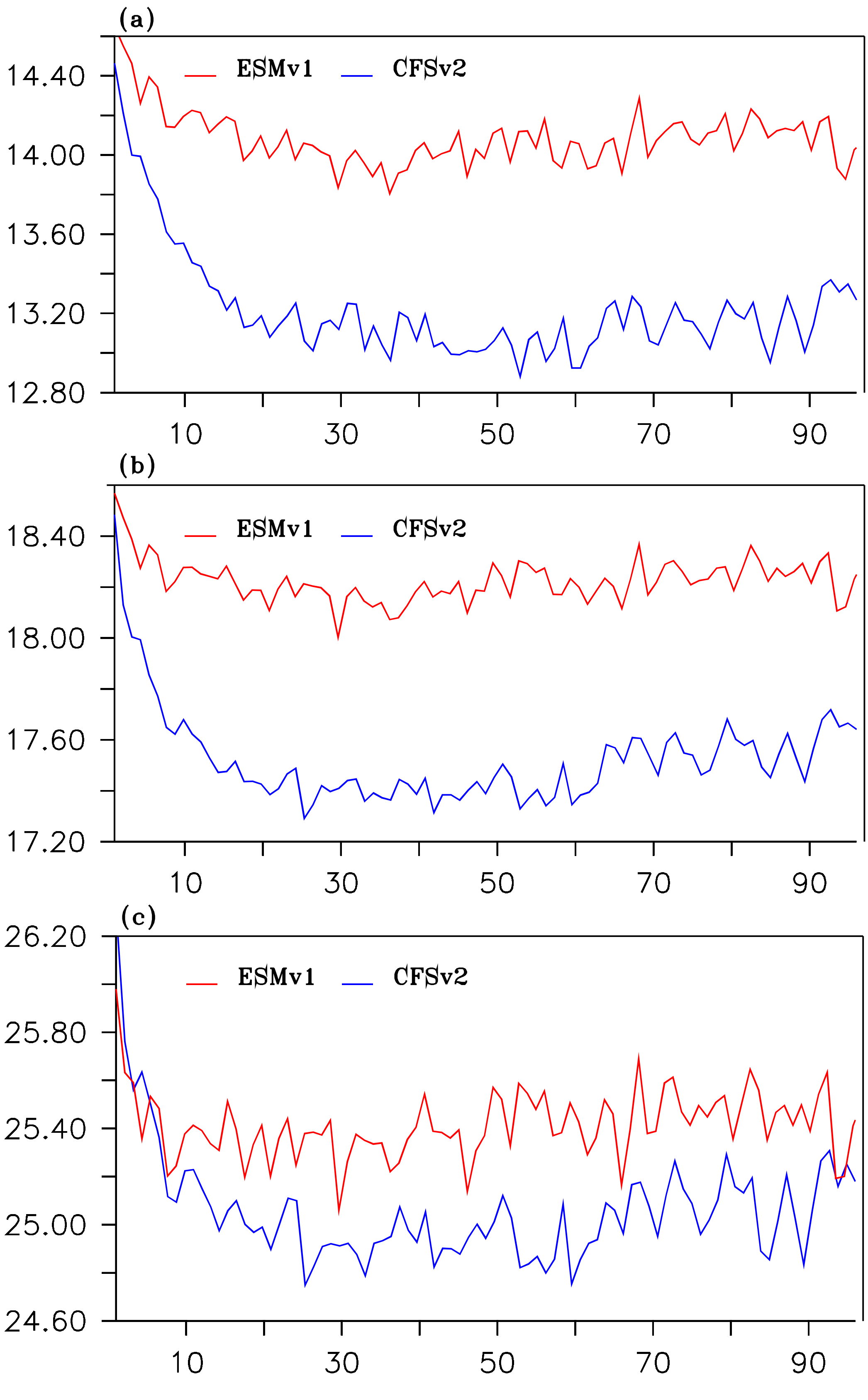

Figure 1. Time evolution of the globally-averaged annual mean fields (°C) of (a) near surface temperature (b) sea surface temperature and (c) tropical sea surface temperature (30°S-30°N). The ESMv1 (CFSv2) simulations are in red (blue). The corresponding annual mean observational values are 14. 6 °C, 18.6 °C and 26.1 °C respectively

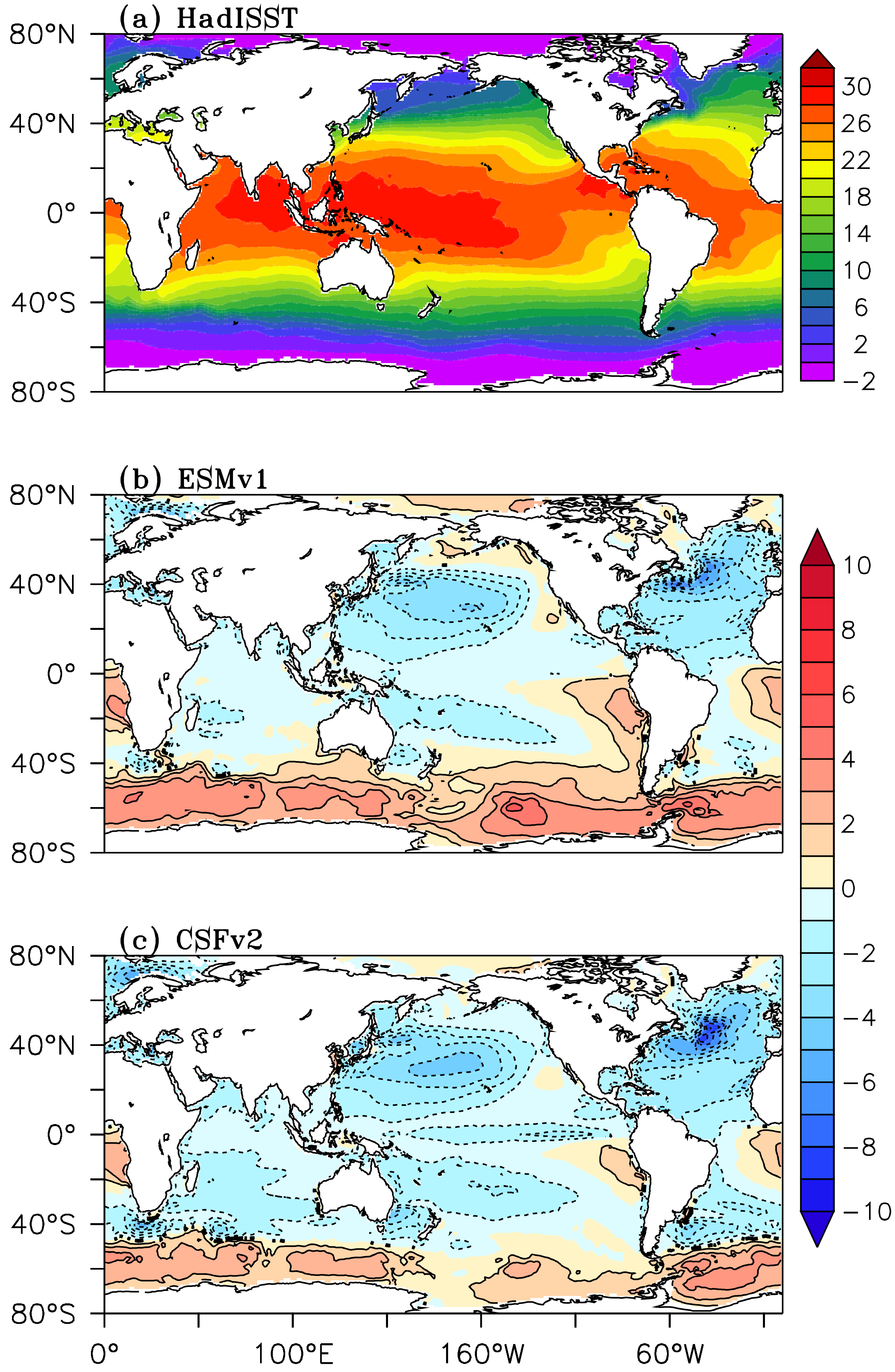

Figure 2. Spatial distribution of annual mean SST (^{o}C) from (a) HadISST and the bias for (b) ESMv1 and (c) CFSv2. The contours represent 10% level of statistical significance based on student's t-test. The rms errors for the ESMv1 are, 1.1 ^{o}C (global), 0.79^{o}C (30^{o}S-30^{o}N), and for CFSv2, 1.1^{o}C (global), 0.89^{o}C (30^{o}S-30^{o}N).

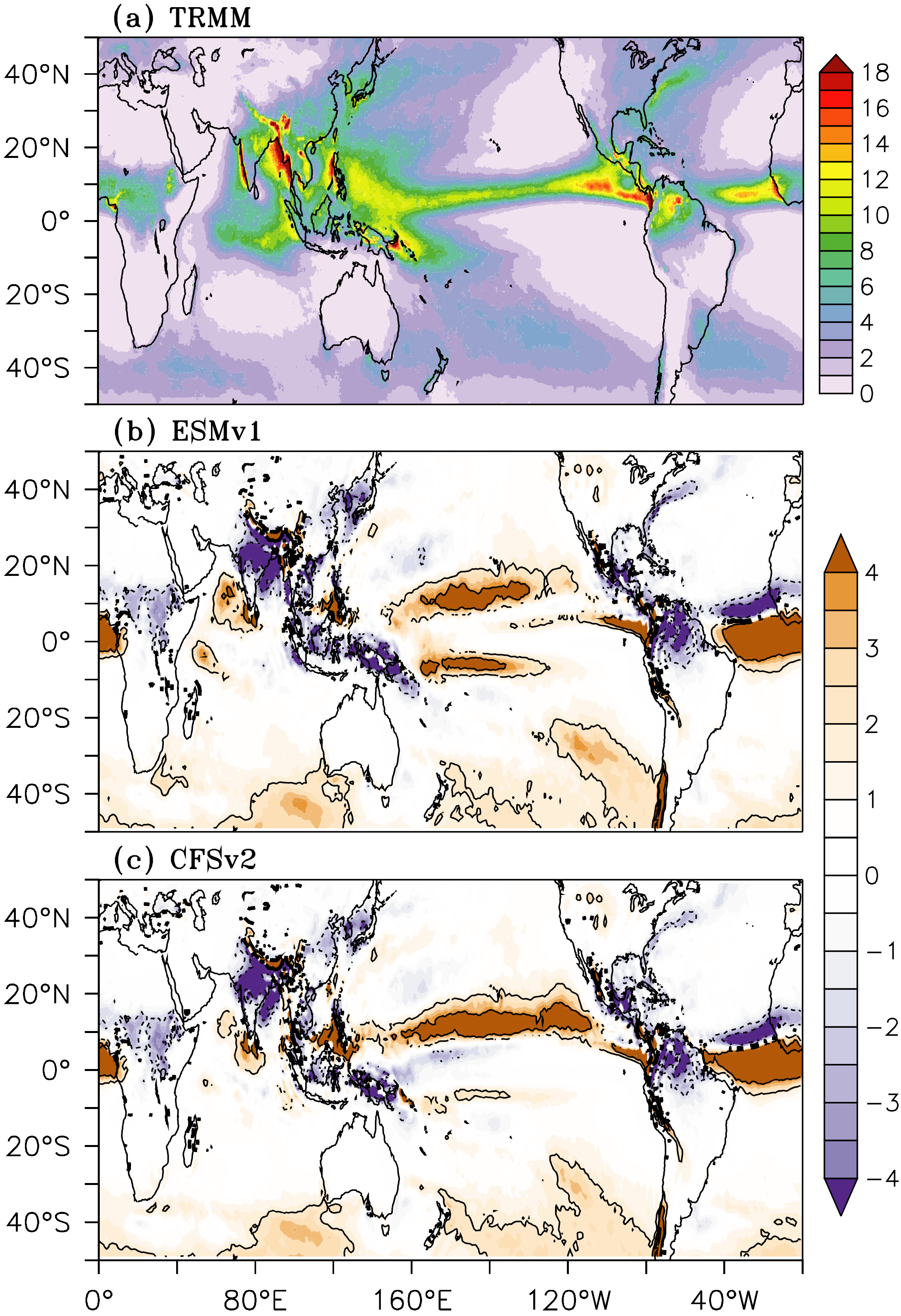

Figure 3. Spatial map of mean summer monsoon precipitation (JJAS; mm day^{-1}) from the (a) TRMM and the biases for (b) ESMv1 and (c) CFSv2. The contours represent 10% level of statistical significance based on student's t-test.

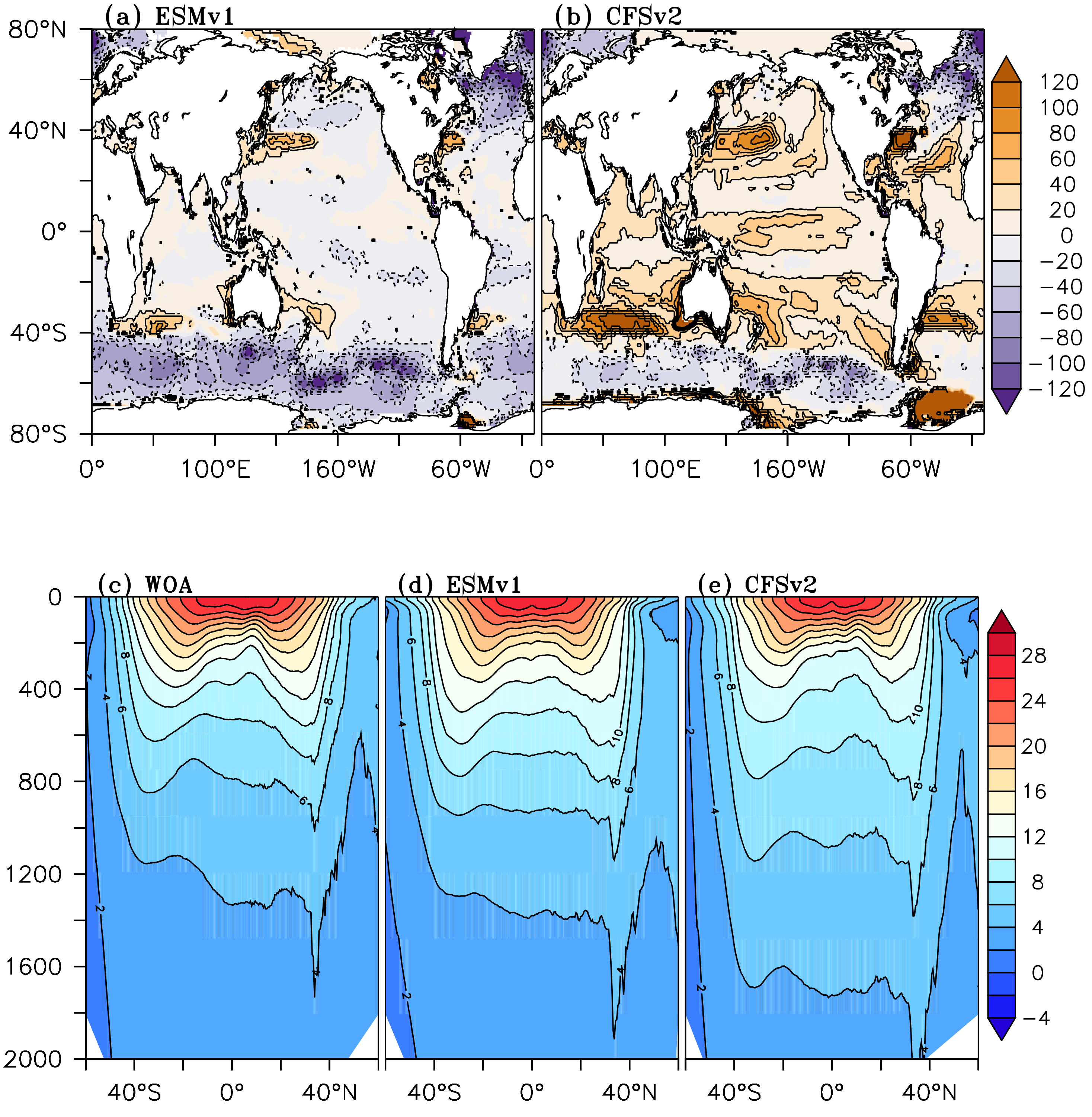

Figure 4a. Spatial maps of bias in annual mean mixed layer depth for ESMv1 and (b) CFSv2. The model results are computed over the last 50 years of simulation. Biases are in meter. The contours represent 10% level of statistical significance based on student's t-test. (c) vertical distribution of the global ocean zonal mean temperature (°C) from WOA (d) and (e) same as (c) except for ESMv1 and CFSv2 respectively.

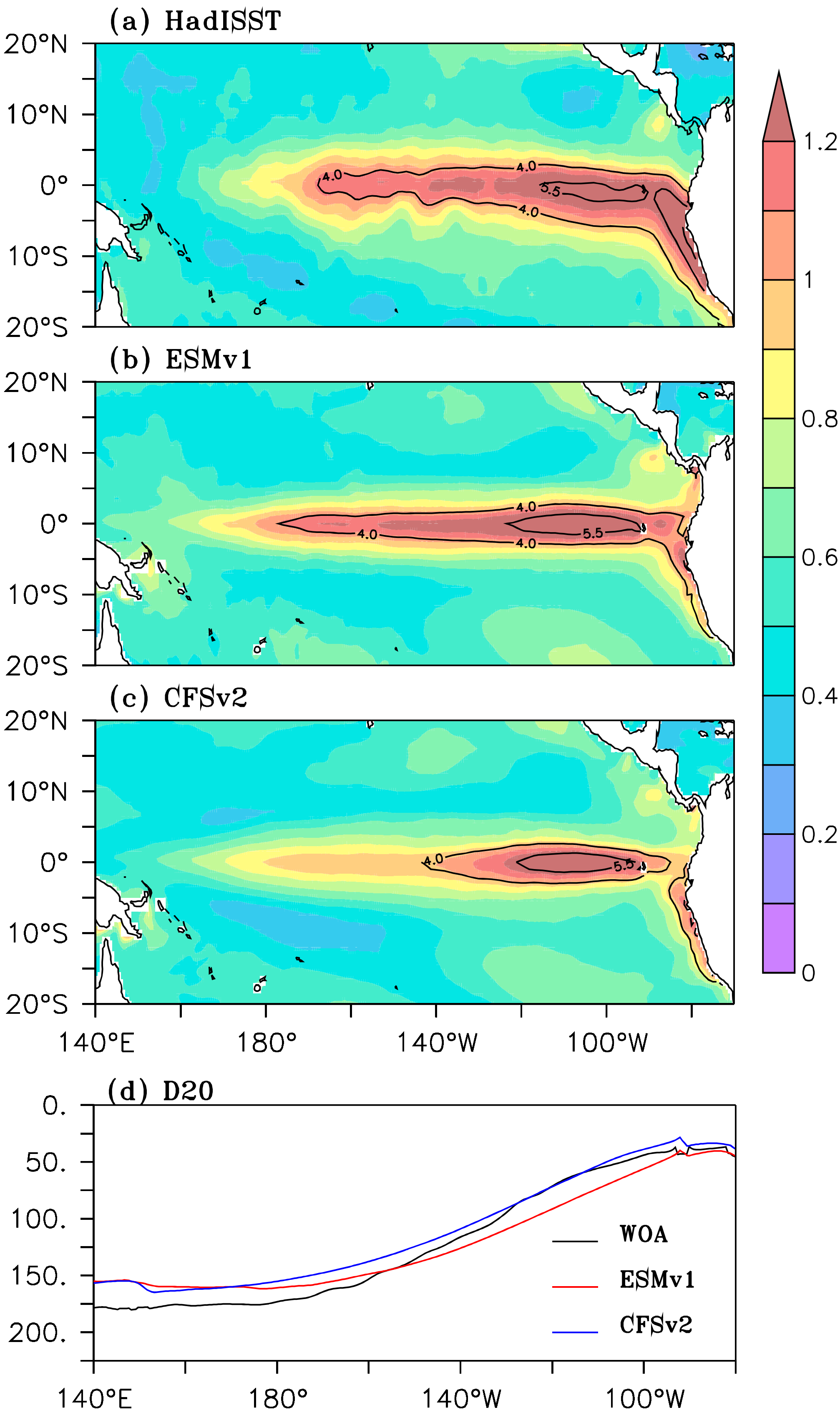

Figure 5. Standard deviation of interannual SST anomalies (°C, shaded) for (a) HadISST (b) ESMv1 and (c) CFSv2. The coefficient of variation (%) are overlaid as contours. (d) depth of 20 ^{o}C isotherm (m) in the equatorial Pacific (5^{o}S-5^{o}N) for WOA, ESMv1 and CFS2

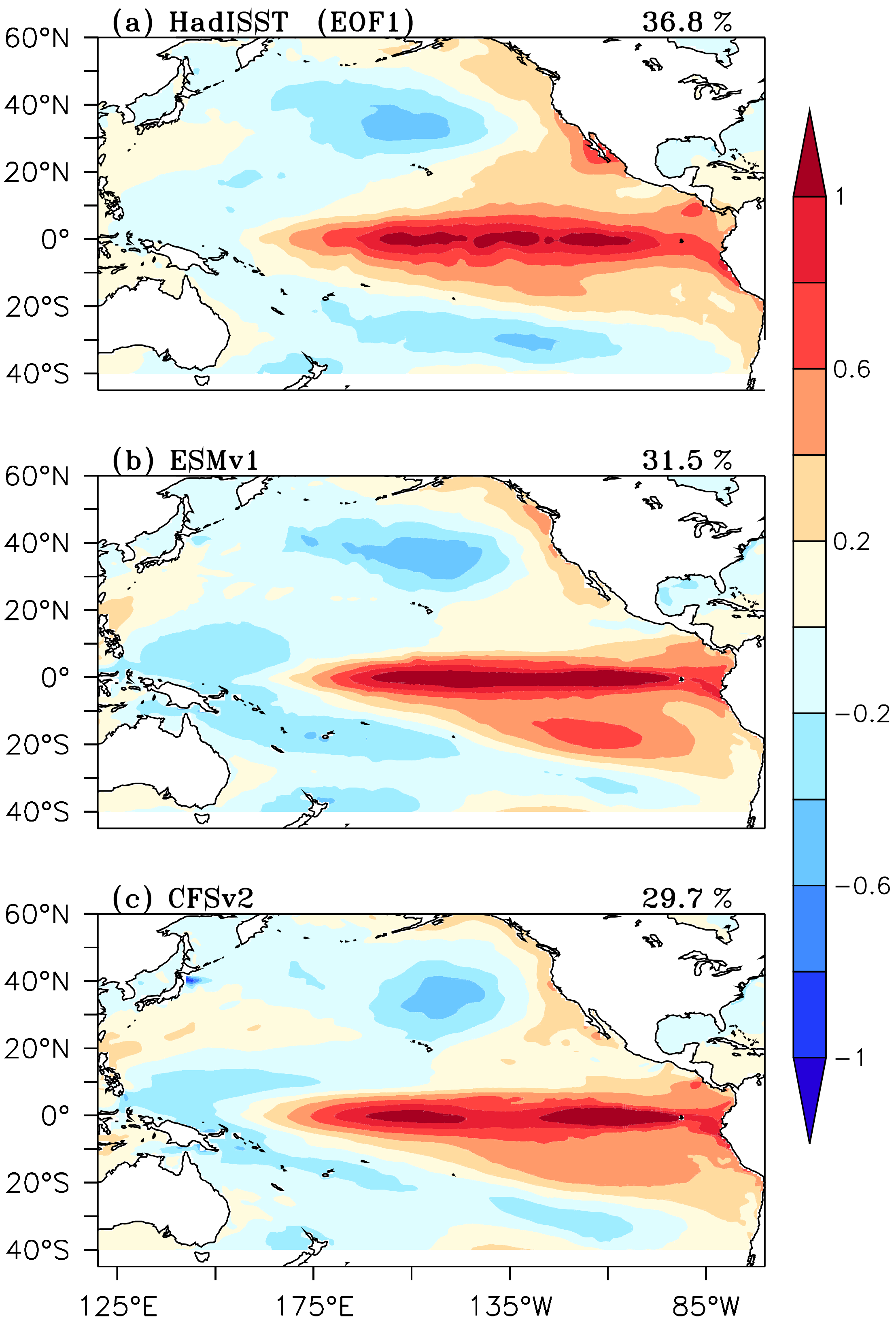

Figure 6. The leading EOF pattern of boreal winter (December-February) SST anomalies (°C) in the pacific for (a) HadISST data for the period 1935-2010 (b) ESMv1 and (c) CFSv2. The model results are computed over the last 75 years of simulations.

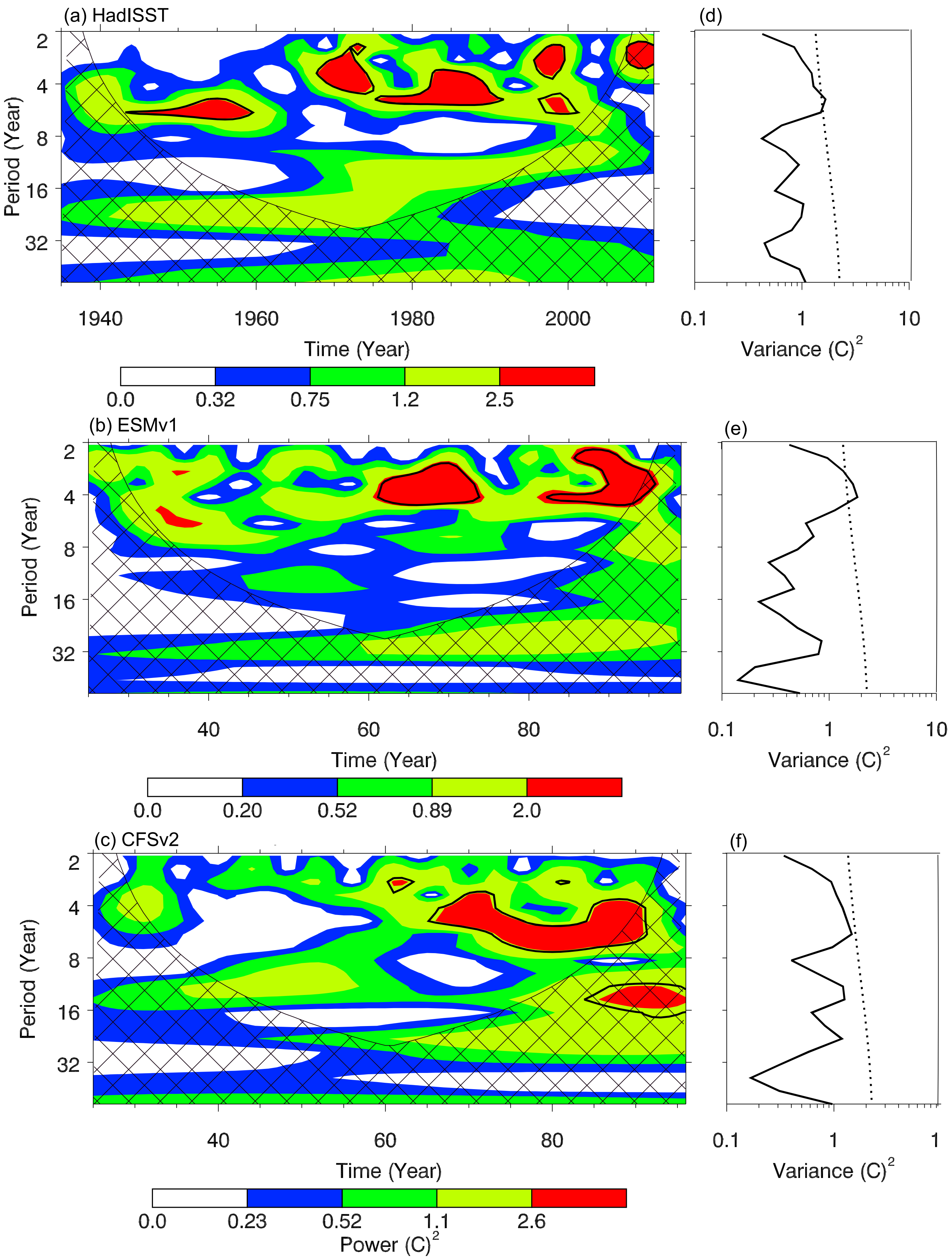

Figure 7. Time series of wavelet power spectra of the gravest principal component from the EOF analysis of the pacific winter SST (120°E-80°W,60°N-60°S; see Fig. 6) for (a) HadISST (b) ESMv1 and (c) CFSv2. Black contour is the 10% significance level. The corresponding time-averaged power spectra are shown for (d) HadISST (e) ESMv1 and (f) CFSv2. The dashed line is the 10% significance for the time-averaged power spectra.

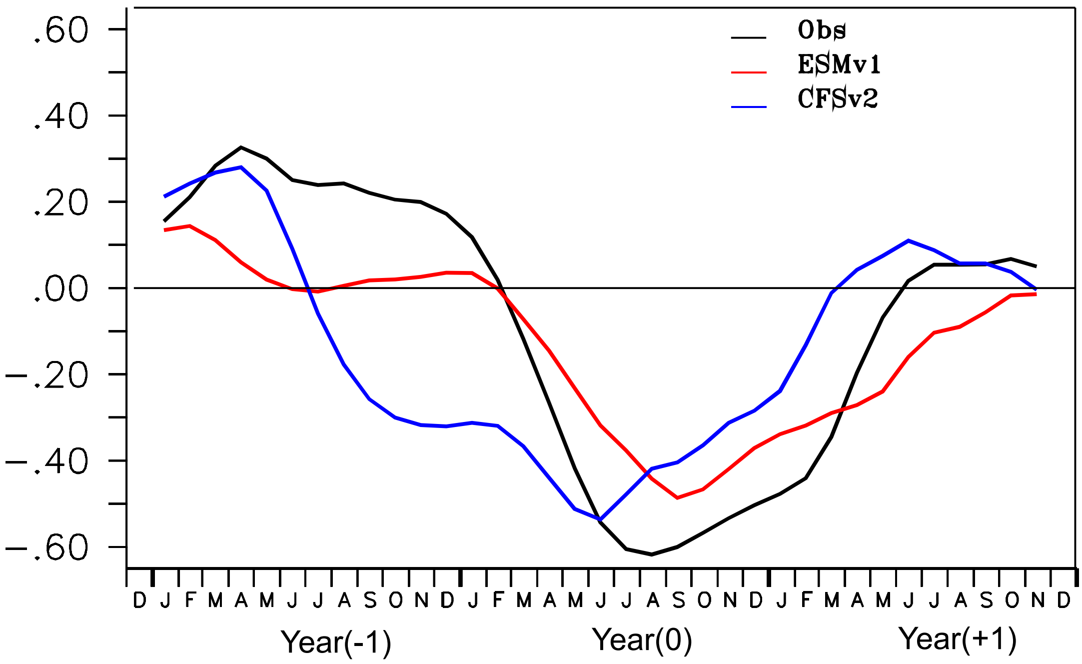

Figure 8. Lead–lag correlations between All Indian Summer Monsoon derived from the IMD datasets (June-September) rainfall and monthly Nino-3.4 index from the HadISST, for the 1935-2010 period (black line), ESMv1 (red line), CFSv2 (blue line). Note that the model results are computed over the last 75 years of simulations for comparison.

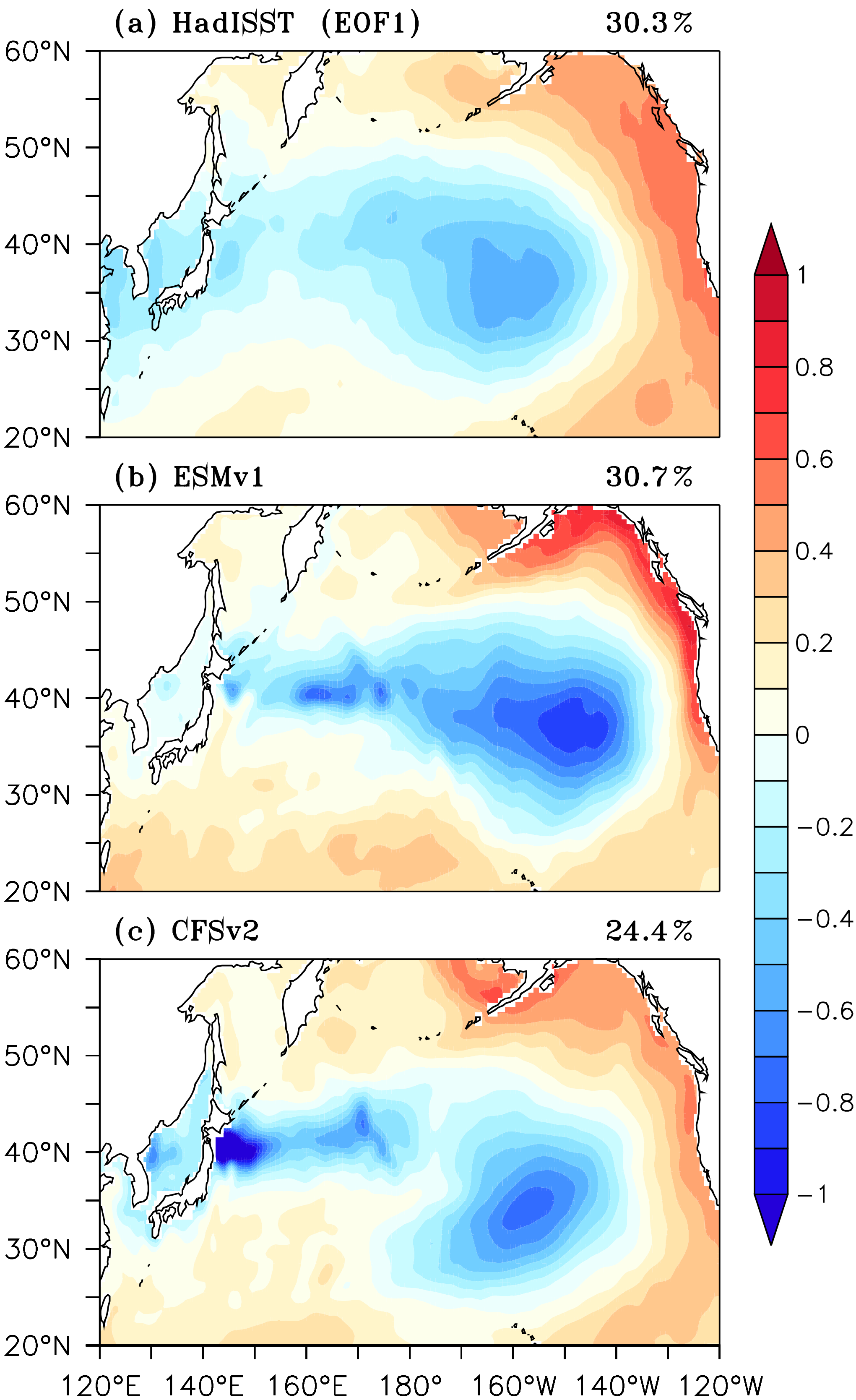

Figure 9. The leading EOF pattern of detrended monthly SST anomalies (°C) in the north Pacific (120°E-120°W, 20°N-60°N) (a) HadISST data for the period 1935-2010 (b) ESMv1 and (c) CFSv2. The model results are computed over the last 75 years of simulations.

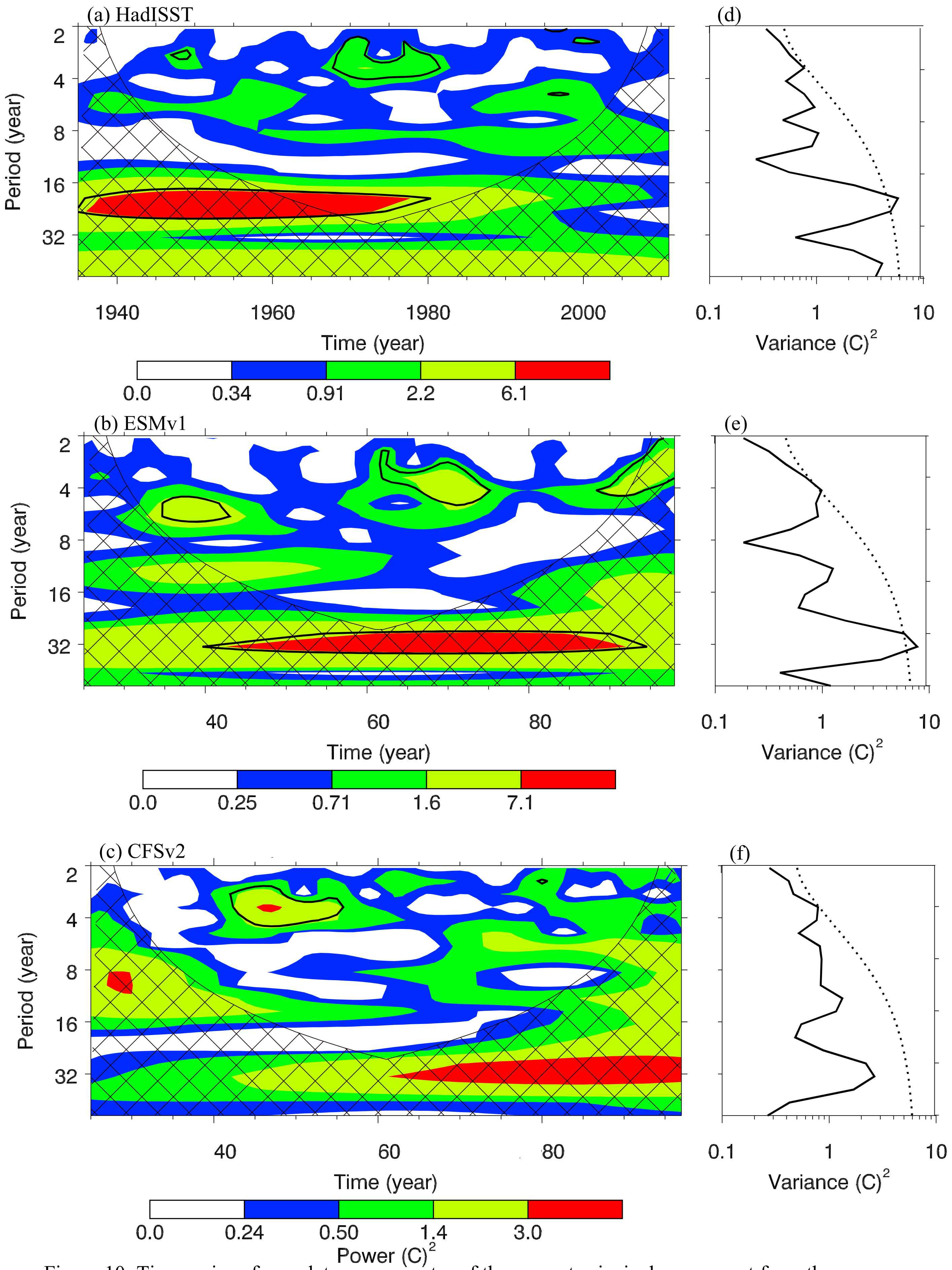

Figure 10. Time series of wavelet power spectra of the gravest principal component from the EOF analysis of the northern pacific SST (120°E-120°W,20°N-60°N; see Fig. 9) for (a) HadISST (b) ESMv1 (c) CFSv2 and the black contour is the 10% significance level. (d) the corresponding time-averaged spectra. The dashed line is the 10% significance for the time-averaged power spectra.

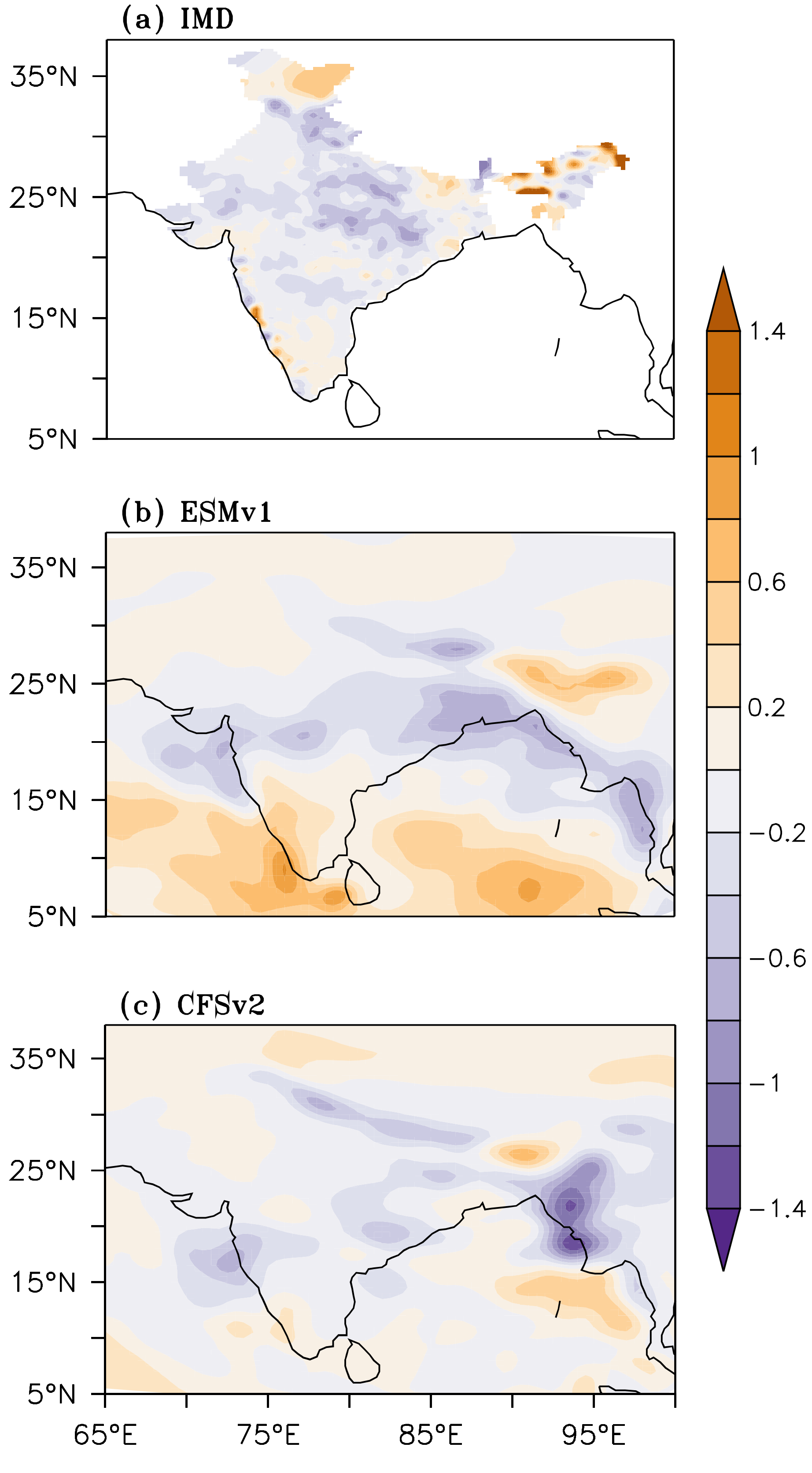

Figure 11. Spatial map of JJAS rainfall anomalies (mm day^{-1}) regressed on to the gravest principal component from EOF analysis of northern pacific (120^{o}E-120^{o}W,20^{o}N-60^{o}N; see Figure 9) from (a) Observations (for the period 1935-2010) (b) ESMv1 and (c) CFSv2. The model results are computed over the last 75 years of simulations.